Title

A Direct Probe of the Hydrogen Bond Network in Aqueous Glycerol Aerosols



Journal

The Journal of Physical Chemistry Letters, 12(23)

ISSN

1948-7185

Authors

Weeraratna, Chaya

Amarasinghe, Chandika

Lu, Wenchao

et al.

Publication Date

2021-06-17

DOI

10.1021/acs.jpclett.1c01383

Peer reviewed

# A Direct Probe of the Hydrogen Bond Network in Aqueous Glycerol Aerosols

**Chaya Weeraratna, Chandika Amarasinghe, Wenchao Lu, Musahid Ahmed***

*Chemical Science Division, Lawrence Berkeley National Laboratory, Berkeley, California 94720, USA*

**Abstract**

The properties of aerosols are of paramount importance in atmospheric chemistry and human health. The hydrogen bond network of glycerol-water aerosols generated from an aqueous solution with different mixing ratios, is probed directly with X-ray photoelectron spectroscopy. The carbon and oxygen X-ray spectra reveal contributions from gas and condensed phase components of the aerosol. It is shown that water suppresses glycerol evaporation up to a critical mixing ratio. A dielectric analysis using terahertz spectroscopy coupled with Infrared spectroscopy of the bulk solutions provides a picture of the microscopic heterogeneity prevalent in the hydrogen bond network when combined with the photoelectron spectroscopy analysis. The hydrogen bond network is comprised of three intertwined regions. At low concentrations, glycerol molecules are surrounded by water forming a solvated water network. Adding more glycerol leads to a confined water network, maximizing at 22 mol%, beyond which the aerosol resembles bulk glycerol. This microscopic view of hydrogen bonding networks holds promise in probing evaporation, diffusion dynamics and reactivity in aqueous aerosols.

**TOC figure –**

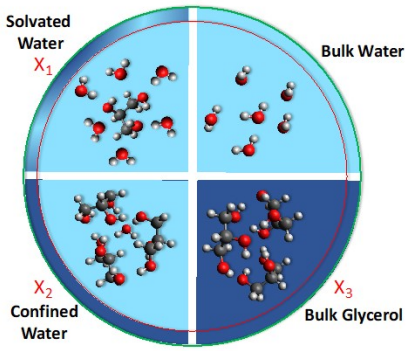

Glycerol, a polyalcohol with three hydroxyl groups connected to a three-carbon chain, is a viscous liquid at room temperature by virtue of forming an intricate network of intra and intermolecular hydrogen bonds. Upon cooling it forms a glassy solid, and is highly miscible in water, whereupon it disrupts water's hydrogen bonding network and suppressed freezing. Thus, its colligative properties allow it to be used as an antifreeze and a cryo-protectant with immense biological ramifications since it allows stabilization of cells and tissues at subzero temperatures.[1] Due to its high miscibility in water, glycerol has been used as a coupling medium for microwave tomography especially important in breast tissue imaging.[2] This aspect of glycerol's impact on the thermodynamic and structural properties of water is also very important in the field of aerosol chemistry. The study of the physical and chemical properties of aerosol droplets to understand the spreading of respiratory illness, particularly COVID, has taken on added urgency due to the ongoing pandemic. These studies focus on virus transmission, lifetime of aerosols suspended in air, effects on human health and barriers to viral transport.[3-5] Moreover, glycerol is the major constituent in e-cigarettes and there is renewed interest in its transport and chemical properties particularly in mixtures with propylene glycol and water, with teenage addiction to vaping.[6-8] From a fundamental view, cooling of glycerol-water mixtures has also been used controversially to report evidence for a liquid-liquid transition in water.[9] Glycerol uptake of water vapor can give rise to very interesting mechanical changes such as a recently reported Benard-Marangoni instability which gives rise to convection cells.[10] The slow rheological dynamics in glycerol water mixtures has been attributed to changes in the hydrogen bonding networks.[11] The effects of glycerol on lipid monolayers via its influence on microbubble formation have been documented using optical microscopies.[12] These aspects of the colligative properties of glycerol solutions are technically and scientifically important for new directions in green chemistry, and thermal science.

It is not surprising that there have been many experimental and theoretical attempts to understand the molecular level details of the hydrogen bond network upon mixing glycerol with water. Seminal work using neutron scattering and molecular dynamics simulations suggests that glycerol and water form clusters which are directed by intramolecular and intermolecular hydrogen bonding

between the two systems.[13-14] This is corroborated by infrared,[15-17] and dielectric[18-21] spectroscopy of water-glycerol mixtures where it is suggested that subtle interactions, between four regimes of hydrogen bonding in bulk glycerol, solvated glycerol, confined water, and bulk water drive the underlying dynamics. However, a molecular-level picture of glycerol water mixtures, particularly in aerosols remains opaque.

In this paper, we present the study of glycerol-water interactions of aerosol nanoparticles utilizing X-ray photoelectron spectroscopy (XPS), performed via velocity map imaging (VMI). Previously, the thermodynamics and kinetics of water uptake on glycerol aerosols[8], liquid marbles,[22] and droplets[23-24] have been studies by probing the evaporation and condensation of water vapor onto dried glycerol systems. To date, while there have been studies of aerosolized propylene glycol, glycerol, nicotine, and water by single-photon ionization mass spectrometry,[25] and laser trapping-Raman scattering,[26] we have not seen a report of an X-ray spectroscopic study of aerosolized glycerol water solutions. The closest equivalent to our experimental work is a vacuum ultraviolet photoionization study of a 500 nm glycerol aerosol (without water) between 10.0 and 13.9 eV where nano-focusing, and shadowing was observed in the photoemission processes.[27] X-ray photoelectron spectroscopy collected at C and O 1s bands provides a surface sensitive probe of the local electronic structure. VMI provides the advantage of simultaneous measurement of photoelectron energy and the angular distribution with $4\pi$ collection efficiency and has been applied to the study of solvation of the amino acids, arginine[28] and histidine,[29] determination of electron scattering dynamics in organic nanoparticles[30] and also to probe the near-edge X-ray absorption fine structure spectroscopy (NEXAFS) of water[31] using a variant of VMI. X-ray photoelectron spectroscopy of alcohol+water solutions[32-34] have been probed using a hemispherical analyzer in conjunction with liquid jets, and ice,[35] while X-ray absorption spectroscopy (XAS)[36-37] and X-ray Raman Scattering[38] has been performed on mono-alcohols. We discuss these results to highlight differences in the evaporative properties of glycerol in contrast to highly volatile alcohols such as methanol, ethanol and propanol probed in liquid jets and thin film surfaces. To complement and understand the differences in the hydrogen bond network upon mixing, we undertook chip-based attenuated total reflection (ATR) IR

spectroscopy and THz-Time Domain Spectroscopy of the same solution mixtures that were used for generating aerosols for the X-ray analysis.

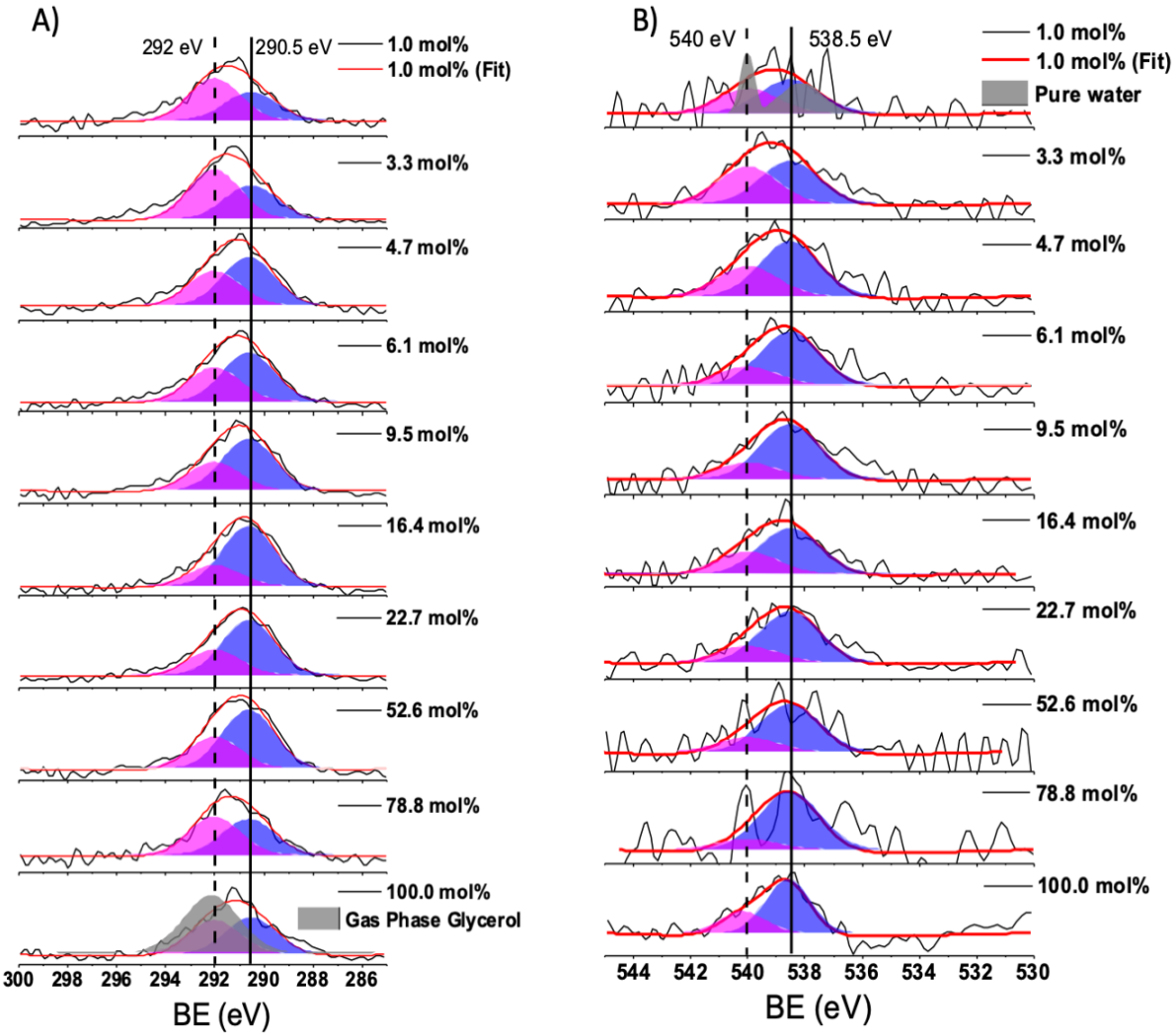


Figure 1: X-ray photoelectron spectra at different glycerol water concentrations. A) C 1s spectra measured at a photon energy of 315 eV. Gray inset at 100.0 mol% is the gas phase spectrum of glycerol, used to disentangle the gas phase (292 eV) and condensed phase (290.5 eV) contribution. B) O 1s spectra measured at a photon energy of 560 eV. A spectrum is superimposed on the 1.0 mol% spectrum showing gas phase (540 eV) and condensed phase (538 eV) peaks of pure water. (From ref. 39) Solid and dashed lines indicate the condensed phase and gas phase BE positions, respectively.

The C 1s and O 1s X-ray photoelectron spectra at different glycerol water concentrations are shown in Fig. 1 (A) and (B) respectively. In the C spectrum, a broad peak is observed between 296-287 eV which should be representative of the glycerol content of the aerosol beam, whereas a similar broad peak is observed between 542-534 eV at the oxygen spectrum and its contribution is from both glycerol and water. The contributions to these peaks will arise from the gas and condensed phase components of the mixture. There has been a limited number of XPS studies of alcohol-water mixtures at the C 1s level utilizing a liquid jet coupled to photoelectron spectroscopy. Since these experiments were performed with highly volatile alcohols, in contrast to glycerol, the gas phase component was comparatively large and dominated the total spectral distribution. Typically, the BE shift between gas and the condensed phase is around ~2 eV with the gas phase having a larger binding energy.[39] In Fig. 1 (A), we fitted the experimental data with two Gaussians to represent the gas (292 eV) and condensed phase (290.5 eV) component and the sum shows the fit to the experimental data reasonably well, apart from the region between 296-294 eV. To account for that, we have used a three-peak fit which is shown in the supplementary information (SI 1). Since both fitting mechanisms generated similar trends, we chose to use the two Gaussian fit. For the O XPS data, peak identification becomes somewhat complicated since O atoms are present in both glycerol and water and our experimental resolution is not adequate for accurate separation of each species. Therefore, our two-peak Gaussian analysis for the gas phase and the condensed phase peaks have the contribution from both glycerol and water. Our analysis is in good agreement with literature [39] in the case of BE shifts and peak positions (540 and 538.5 eV) when we compare the gas and condensed phase component as shown for pure water superimposed on the 1 mol% data of the O 1s spectrum. Given our experimental resolution, we focus on the intensity changes as a function of glycerol mol% fraction, rather than BE shifts, to gain insight into the change in the hydrogen bond network.

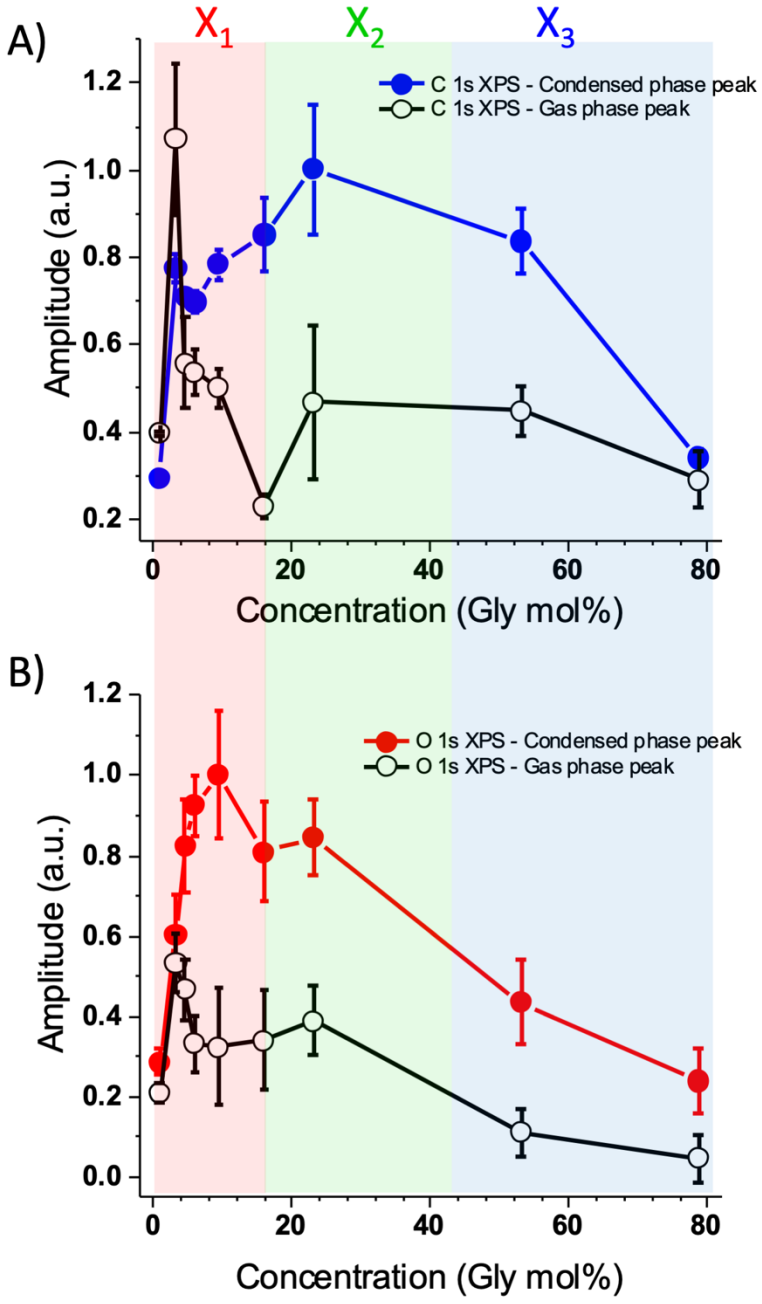


Figure 2: Condensed phase (filled circles) and gas phase (open circles) XPS intensities as a function of Glycerol mol%. (100 mol% glycerol intensity is not reported here since its aerosol generation mechanism is different to glycerol-water mixtures.) A) C 1s XPS peak intensities B) O 1s XPS peak intensities. Three regions corresponding to glycerol-water networks are indicated in colored regions, red ($X_1$) is solvated water, green ($X_2$) is confined water and blue ($X_3$) is bulk glycerol network.

By obtaining the amplitudes of the peaks shown by the Gaussian distributions in Fig. 1 and plotting them as shown in Fig. 2 (A) and (B), we can extract the changes in condensed and gas phase contributions at the C and O 1s levels respectively as a function of concentration. First, we will focus our discussion on the condensed phase contribution. In the C distribution, the intensity shows a sharp rise from 1 mol% to 23 mol% and then gradually drops down in intensity to 78 mol% concentration. In the O intensity distribution, shown in Fig. 2 (B), the peak rises steadily between 1-9.5 mol%, drops at 16 mol%, then a small rise until 23 mol% and then continues to drop in intensity. These trends will be compared to a series of experimental results performed on highly volatile alcohol + water solutions in liquid jets[32-34] to discern systematic differences between aerosols and liquid jets, and the viscous nature of glycerol with its low vapor pressure. While there has been a number of studies, we will compare our results with those obtained by Marinho et al. for ethanol + water solutions since they have measured C XPS spectra in the molar range similar to us.[34] They used a standard Langmuir adsorption model to fit their condensed phase C XPS data till around 14 mol%, which is similar to what we have observed for our data till 25 mol% concentration (SI 2). This means that our aerosol beam beyond 20 mol% starts to drop in signal in contrast to the liquid jet data and reflects the fact that aerosol size and/or concentration drops dramatically beyond 20 mol%. Evidence for such behavior has been shown in the literature where Wright et al.[8] using particle sizing methods showed that in dry environments, glycerol aerosols evaporate rapidly, while under humid conditions, they tend to stabilize. Therefore, we could justify that the intensity drop at higher glycerol concentration is due to enhanced evaporation of the glycerol molecules. When water is added, it results in mutual depression of vapor pressures slowing down the glycerol/water evaporation.

Interesting trends can be seen at the low glycerol concentrations (< 30 mol%). As mentioned earlier, the C intensity distribution has one prominent peak at 23 mol% and O shows two peaks at 9.6 mol% and 23 mol%. These features could be due to changes in hydrogen bonding network as we change the glycerol-water composition. A parallel trend was observed in the dielectric and THz study performed by Vinh and coworkers,[21] in aqueous solutions of glycerol. In that work, four hydrogen bonding networks were proposed, bulk water, solvated water, confined water and bulk glycerol. Later,

we will describe THz and IR measurements performed here which corroborate and set the stage for the description of the hydrogen bond network observed in the mixtures. First, we will consider the bulk water system where all hydrogen bonding is between water molecules, and when we start adding glycerol, they initially accumulate in the hydration layer. Since each glycerol can bond with 6 water molecules, the number of waters in the hydration layer also gradually increases forming a layer of solvated water. From dielectric relaxation calculations, a critical glycerol concentration of ~7.5 mol% was obtained as the maximum number of water molecules in the hydration layer,[21] whereas in the O 1s XPS, the first major feature observed at 9.5 mol% probes this solvated water network (region $X_1$ in Fig. 2). As we continue to add more glycerol into the mixture, water will get replaced by glycerol molecules forming predominantly a network of glycerol with confined water (region $X_2$). A second, less intense feature observed at 23 mol% is attributed to this glycerol-water network. The low intensity of the signal can be explained by having the O atom contribution only from glycerol, since water is embedded inside the glycerol cluster and XPS is only sensitive to the surface. For the C XPS intensity, the peak at 23 mol% matches with O XPS intensities further justifying our explanation. After, 23 mol%, at high glycerol concentrations, the system mostly behaves as bulk glycerol (region $X_3$) and the O XPS intensity gradually decreases due to low number density of the aerosol particle owing to evaporation.

Furthermore, we investigated the gas phase intensity trends to gain insight on the evaporative behavior of the aerosols upon addition of glycerol. Both the C and O XPS intensities initially peaks at 3 mol% then gradually decreases and a low peak is observed at 23 mol% before continuing to decrease until 78 mol%. We can use this information to obtain qualitative insight into the local evaporation rate at the interaction region. According to Wright and coworkers, dry glycerol aerosols are more volatile and in glycerol-water mixtures, mutual depression of vapor pressure slows the glycerol evaporation.[8] Hence vaporization during the travel from the atomizer to the interaction region can lead to shrinking and loss of aerosol mass. Initially since water stabilizes the glycerol evaporation, particle size at the interaction region is comparable to the particles produced by the atomizer (~200 nm). Hence, aerosols at low concentrations have higher surface area and as we increase the glycerol mol fraction, evaporation rates go up which in turns reduces the particle size. The increased intensity

seen at 3 mol% is due to the larger surface area of the particles at the interaction region and evaporation decreases as particles shrink. The second peak in the intensity distribution at 23 mol% marks the boundary (X2/X3) between confined water/solvated glycerol and bulk glycerol. Beyond that, at higher glycerol concentrations even though the evaporation rates go up, most of the glycerol molecules will be lost in the transfer lines and smaller sized aerosols will be left in the interaction region reflected in the observed low gas phase signal. Our analysis is also corroborated by a near edge X-ray absorption fine structure (NEXAFS) analysis (SI 3) performed during the course of our XPS measurements. We chose to work with the O edge since this provides information for both glycerol and water concentration in the aerosol beam and NEXAFS in contrast to XPS is bulk sensitive. The total signal rises rapidly, peaks at 9.5 mol%, drops and plateaus between 23-45 mol% and then rapidly drops, reflecting the evaporation of the glycerol aerosol with decrease in water content. While NEXAFS has been used in the literature to describe hydrogen bond networks in aqueous alcohol systems,[37, 40] we have refrained from such an analysis. We believe that the XPS analysis combined with the IR and THz data described below, provides a clearer picture of the hydrogen bond networks prevalent in the system.

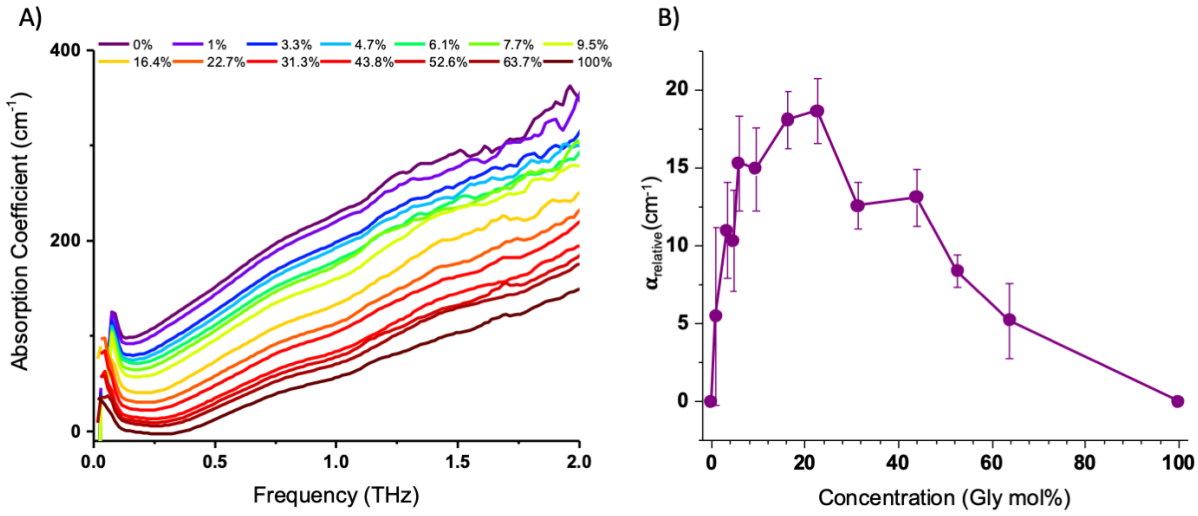


Figure 3: THz spectra at different glycerol water concentrations. B) $\alpha_{relative}$ plotted against glycerol concentrations.

As described earlier, we conducted THz-TDS measurements of the solutions to discern the hydrogen bond network patterns suggested by the XPS analysis and dielectric studies mentioned in the literature.[31] The advantage of the THz-TDS technique is that it provides both intensity and phase information of the signal and measures the real and the imaginary part of the refractive index simultaneously. Therefore, we can calculate the absorption coefficient and extract the dielectric response directly from the THz spectrum.

The absorption coefficient results from our measurements are shown in Fig. 3. The absorption spectra show a monotonic increase with frequency and upon addition of glycerol leads to a reduction in the absorption. Since the relative amount of water absorption decreases as the glycerol mole fraction increases, a volume mixing model[41-42] can be used to connect the observed absorption to a relative one via the following relation.

$$\alpha_{ideal}(\omega) = V_w \alpha_w(\omega) + V_g \alpha_g(\omega)$$

Where,

$$\alpha_{relative} = \alpha_{ideal} - \alpha_{real}$$

Here $V_w$ and $V_g$ are volume fractions of pure water and pure glycerol, $\alpha_w$ and $\alpha_g$ are the absorption coefficients of pure water and pure glycerol, respectively and $\alpha_{real}$ is the absorption coefficient of the glycerol/water solution mixture measured experimentally. Given the relative lack of features in the THz spectra, we calculated the averaged $\alpha_{relative}$ values at 0.498, 1.011 and 1.260 THz. In Fig. 3 B), is plotted $\alpha_{relative,}$ the positive value of which indicates the deviation of the mixture from ideal mixing. This is because, glycerol is disrupting the hydrogen bonding network of water and forming new structures as suggested earlier[21] and has maximum around 23% mol concentration.

The dielectric response of a system provide insight into the dynamical behavior of liquids at a molecular level. Depending on the amount of glycerol and water in the system, the rotational relaxation mechanism of these mixtures will be different and can be divided into four modes: bulk water, bulk

glycerol, solvated water and confined water.[21] By calculating the complex-valued dielectric constant and fitting into a Debye-type model, the contribution from each of these relaxation processes to the total complex dielectric constant can be extracted. Contributions from each mechanism plotted as a function of glycerol concentration is shown in Fig. 4. The method of dielectric analysis is presented in the supplementary information (SI 4).

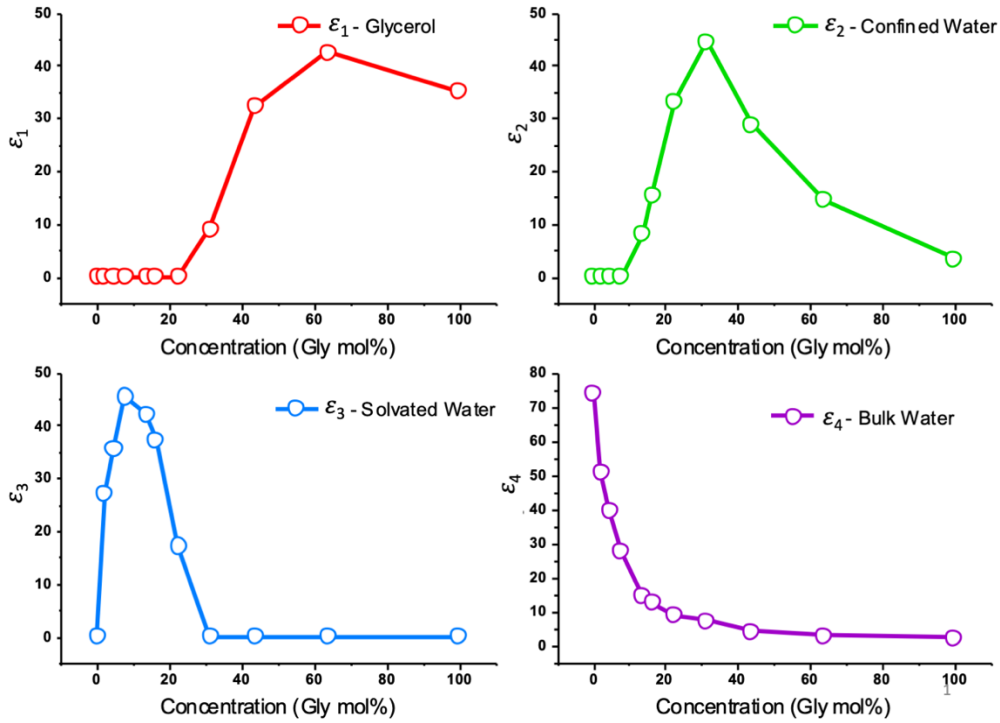


Figure 4: Dielectric relaxation trends with concentration for each relaxation process. $\varepsilon_1$ for bulk glycerol, $\varepsilon_2$ for confined water, $\varepsilon_3$ for solvated water and $\varepsilon_4$ for bulk water relaxations.

The excess molar volume (EMV) or the $\alpha_{relative}$ of the system represents new hydrogen bonds formed that are different from the hydrogen bonding network of pure glycerol and water, which arises from mixing. In our system, only solvated water and confined water can give rise to a positive EMV. Hence, we compared the sum of solvated and confined water contribution to the dielectric response with the EMV trend that was shown in Fig. 3 B) which showed an excellent agreement (shown in Fig. S4). This gives us confidence that the fitting procedure we used for extracting the dielectric constants is accurate and can be used to confirm our XPS data.

According to the dielectric trends in Fig. 4, solvated water peaks at 7.8 mol% and confined water peaks at 31 mol% is in excellent agreement with the two features observed in the XPS results. XPS is sensitive to the surface layer of the aerosol, hence, contribution to the condensed phase signal of water in O 1s XPS can only come from solvated water. Thus, $\varepsilon_3$ and pure water O intensities should have a similar distribution. O condensed phase signal has contribution from both pure water and glycerol, and only glycerol will contribute directly to the C XPS signal. Therefore, to extract the trend of water contribution to O 1s XPS signal, O XPS intensity distribution was divided by the C XPS intensity distribution. We emphasis here that the resulting distribution is purely a trend to compare with the dielectric analysis rather than the absolute water contribution. As shown in Fig. 5, almost a perfect match can be seen except for 78 mol% which could be due to the low and noisy O signal from enhanced evaporation of the aerosol with low water content (95% glycerol by volume). The THz dielectric analysis provides a validation of the mechanisms we proposed for the aerosol mixtures using XPS.

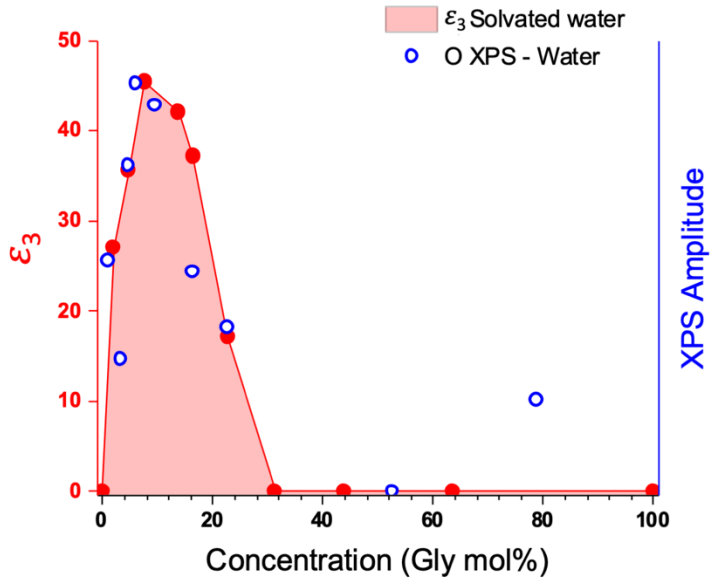


Figure 5: Comparison of dielectric relaxation trend for solvated water ($\varepsilon_3$) with O 1s XPS intensities of water extracted by normalizing total O signal from C signal.

IR spectroscopy has been used extensively as a tool to understand the local hydrogen bonding network of glycerol-water solutions[16-17, 43] and coupled to the results identified by XPS and THz spectroscopy will allow us to model a molecular picture of glycerol-water interactions. Fig. 6 shows the IR spectra for glycerol-water mixtures and wavenumber shifts as a function of concentration for four important vibrational modes, OH vibration, CO stretching, asymmetric and symmetric $CH_2$ modes, that provide signatures on the hydrogen bond network.

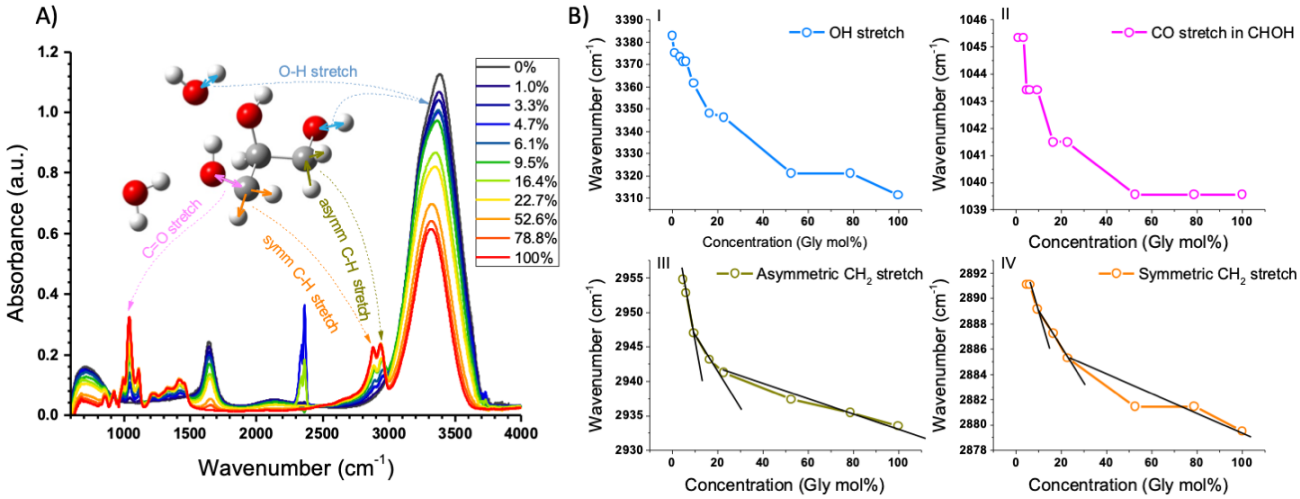


Figure 6: A) ATR-IR spectra obtained for different glycerol-water concentrations. B) Wavenumber trends for 4 vibrational modes I) OH stretching band II) CO stretching, III) asymmetric $CH_2$ stretching and IV) symmetric $CH_2$ stretching.

The OH vibration contains information from both glycerol and water, and in earlier studies, this band has been fitted to three Gaussians to disentangle long, medium and short hydrogen bonding contributions. We did not perform such a fitting procedure, rather we compare our trends to literature to discern the interactions.[43] Short hydrogen bonds are formed between water with inner CHOH and outer $CH_2OH$ of glycerol while long hydrogen bonds are formed with outer $CH_2OH$ groups. At high concentrations, more intermolecular interactions are formed between glycerol molecules and spectroscopy indicates bonds are formed between H of $CH_2$ and O of COH. A clearer picture emerges by examining the $CH_2$ stretching modes which show glycerol backbone interactions. The wavenumber changes with concentrations show a red-shift with increasing glycerol which indicates stretching/weakening of the bond due to weak hydrogen bonding with water and/or another glycerol.

Studies have shown that glycerol backbone bonding with water results in higher red-shift than bonding with another glycerol molecule.[16] The $CH_2$ wavenumber trends in our study can be separated into three slopes shown with solid black lines in Fig 6. B) III and IV. In the first region (4 – 9.5 mol%), a steeper slope can be seen, here glycerol is solvated by water and backbone $CH_2$ groups can form weak CH---OH bonds. In the second region (9.5 – 22.7 mol%), the slope reduces indicating weakening of the hydrogen bonding caused by water being replaced by glycerol molecules in the confined water network. At this point, water tends to bond more with the glycerol hydroxyl group and weaker glycerol OH groups form interactions with the alkyl backbone. Finally, a smaller change is seen by adding more glycerol into the system forming glycerol clusters in the bulk glycerol network.

We have used a novel experimental approach combining X-ray photoelectron spectroscopy of aqueous aerosols coupled with THz and IR spectroscopy of solutions to understand the inter and intramolecular hydrogen bonding network of glycerol-water mixtures. The picture that emerges, is one of three regions of intertwined hydrogen bond networks that percolate these aqueous aerosols. XPS provides properties of the aerosols of these solutions, particularly the surface of the aerosol and THz captures bulk properties. By comparing trends in the XPS intensity with that in the dielectric relaxation extracted from the THz data, we can deduce that there is a homogenous mixing in the aerosol, i.e. there is no difference in the surface and bulk composition. Then we could separate the glycerol-water hydrogen bonding network into three regions depending on the concentration. At low glycerol concentrations, glycerol initially accumulates in the hydration layer forming a layer of solvated water. As the concentration increases, adding more glycerol into the mixture, water will get replaced by glycerol molecules forming a network of glycerol with confined water. At high concentrations of glycerol, the system mostly behaves as bulk glycerol.

To conclude, we have demonstrated that X-Ray spectroscopy of organic aqueous aerosols coupled with THz and IR spectroscopy of the solution from which they are generated provides information on phase changes and hydrogen bonding networks. From an experimental viewpoint, our ability to generate X-Ray spectra from organic aerosols will be of interest to the theoretical chemistry

community.[44] While, theoretical simulations have reached a level of maturity for valence excitations in aqueous systems,[45] there is enormous interest in developing new methods when it comes to core level spectra.[46] Correlations between X-Ray and vibrational spectroscopy at the theoretical level, using the same models of hydrogen bonding networks observed here, will provide a new way to develop an understanding of electronic structure in aqueous organic aerosols.[40, 47-48]

We believe this methodology will find applications in fields as diverse as atmospheric chemistry, thermal science, respiratory disease and optical sensing, where an understanding of hydrogen bond networks is crucial. Phase changes that occur in multiphasic systems can be tuned by invoking non-covalent interactions that are available in hydrogen bonding liquids, plastic crystals, non-crystalline metal organic frameworks, and deep eutectic solvents. Our study of glycerol water aerosols can act as a template to develop a understanding of the molecular heterogeneities that occur upon their interaction in aqueous co-solvent systems[49] and application of external energy inputs, particularly temperature.[50] These systems show significant deviation from ideal behavior upon mixing with solvents, and ions in the bulk environment which is directly a result of micro heterogeneity and liquid-liquid phase separation and solid-solid phase changes respectively. This complex behavior provides a rich tapestry to test hydrogen bond dynamics, probe solvation and confinement and map nucleation and crystallization events.

The ability of XPS to probe the surface region of an aerosol, and the possibility to depth profile also allows us to begin to think about applications of our methodology to probe reactive encounters on aerosols to provide insight into diffusion dynamics and phase separations and their effect on reactivity.[51] A recent topic of much interest to the aerosol and droplet community is the acceleration of reactions in micro-compartments, particularly in microdroplets.[52] The mechanism of this acceleration is hotly debated and the effect of gas phase reactions, evaporation of solvent and phase separations need to be understood in this highly reactive environment.[53-54] Here, the ability to separate gas and condensed phase components of organic aerosols will be useful in providing insight into transport and reactivity in aerosols.

**Experimental Methods**

*X-ray photoelectron spectroscopy:* The aerosol XPS study is conducted at the soft X-ray beamline (9.0.1) of the Advanced Light Source synchrotron facility at Lawrence Berkeley National Laboratory. Detailed explanation of the experimental apparatus has been reported in our previous publications.[31] A short description of the technique will be provided here.

The aerosol beams are prepared by two methods, atomization for glycerol-water mixtures and homogeneous nucleation for pure glycerol. The high viscosity of pure glycerol prevents it from atomizing, therefore the aerosol beam is produced by heating the nucleator oven containing pure glycerol (Sigma Aldrich ≥99.5% purity) to 116 ºC and flowing 400 sccm dry $N_2$ through it. For glycerol/water mixtures, a constant output atomizer is used. A stream of high velocity $N_2$ gas (20 psi) with the flow rate of ~3 l/min is used to atomize these liquid samples. Finer aerosol particles are carried to the vacuum chamber through the exit tube and particles of bigger size are drained back. Glycerol-water solutions are prepared by volume which translate to following concentrations by mol%, 1.0, 3.3, 4.7, 6.1, 9.5, 16.4, 22.7, 52.6 and 78.8 mol%. These aerosols are then introduced into the aerodynamics lens system through a 200 $\mu$m nozzle and focused on the interaction region of the VMI spectrometer. C 1s and O 1s XPS are collected with 315 eV and 560 eV photon energies, respectively. Gas phase signal is collected for glycerol by offsetting the aerodynamic lens position, so that the photon beam only hits the gaseous layer outside the aerosol particles. This experiment is only done for C 1s level due to the low photon flux in the O 1s region.

The VMI apparatus consists of three differentially pumped regions. The aerodynamic lens system (ADL) resides in the first two regions and the third region accommodates the VMI photoelectron spectrometer. The differential pumping regions are used to maintain the pressure inside the reaction chamber at $10^{-6}$ Torr when the aerosol beam is on. The ADL system is capable of focusing a 50 nm – 1$\mu$m aerosol beam into a narrow particle beam thus increasing the flux. The VMI spectrometer comprises 4 electrodes, namely repeller (El4), extractor (El3), and two additional lenses (El2 and El1) to improve the resolution. A potential gradient is provided to these optics for sharp velocity focusing

and time-of-flight expansion of the electron cloud. The optimum potentials used in the current experiment were, El4 = 4000 V, El3 = 3675 V, El2 = 2525 V and El1 is at ground. With these potentials, electrons with kinetic energy up to 50 eV can be detected with the energy resolution of ~2 eV. Electrodes are protected from the external magnetic fields by a mu-metal shield. These photoelectrons are then accelerated toward the position sensitive microchannel plate (MCP) detector and the amplified electron cascade from the MCP hits the phosphor screen illuminating it. The MCP is operated at 1850 V (MCP back plate) and 0 V (MCP front plate) and the phosphor is operated at 4800 V. The light generated by the phosphor screen is detected by the CMOS camera and recorded by a Lab VIEW program. For XPS, two sets of images are acquired, one is the signal when the aerosol beam carries the sample, the other one is the background signal when the beam goes through the inline particle filter. Then the background is subtracted from the signal to get the true sample image. This image is reconstructed by the pBASEX algorithm to get the photoelectron spectrum and the angular distribution information.[55] The photoelectron spectra are calibrated using $N_2$ gas at different photon energies.

*Terahertz Time Domain Spectroscopy (THz-TDS):* The THz-TDS was carried out using a Menlo Tera K15 THz laser system in the transmission mode using the same solutions that were utilized in the VMI-XPS study and some additional concentrations. The measurement was done using a Specac Omni cell with the sample placed between two 3 mm thick polythene windows with a 200 μm spacer. Sampling was performed via averaging for 4 minutes and a reference measurement was taken with an empty cell before each sample measurement. The results were then analyzed and the absorption coefficient and the refractive index for each sample was recorded from 0-3 THz.

*Infrared-Attenuated Total Reflection (IR-ATR) Spectroscopy:* The FT-IR spectra were collected using a Bruker VERTEX 70 FT-IR spectrometer equipped with a silicon-based attenuated total reflectance (ATR) device commercially available from IRUBIS. The ATR crystal is single-bounce, and the inner angle of incidence is 26.7° degrees (corresponding to 20° of outer angle of incidence, optimized by the manufacturer). During operation, several drops of glycerol-water solutions of different concentrations were added to the ATR chips. A well-shaped cover is mounted on top of the ATR

crystals, sealed by a 9 mm O.D. × 7 mm I.D. O-ring that allows for a constant contact area between the ATR crystal and glycerol-water solutions. The spectral scan range was set to 600 – 4500 $cm^{-1}$, with a resolution of 4 $cm^{-1}$. Each spectrum was averaged by 64 scans. Successively, the obtained ATR FTIR spectra were corrected using advanced ATR correction function in OMNIC software package (Thermo Scientific).

**Supporting Information**

1. FITTING OF THE C 1S X-RAY PHOTOELECTRON SPECTRA TO 3 GAUSSIANS
2. LANGMUIR FITTING
3. NEXAFS SPECTROSCOPY
4. DIELECTRIC RELAXATION MEASUREMENTS
5. TABLES (XPS INTENSITIES, $\alpha$RELATIVE, DIELECTRIC CONSTANTS, IR WAVELENGTH SHIFTS)

**Acknowledgement**

This work is supported by the Condensed Phase and Interfacial Molecular Science Program, in the Chemical Sciences Geosciences and Biosciences Division of the Office of Basic Energy Sciences of the U.S. Department of Energy under Contract No. DE-AC02-05CH11231. This work used resources of the Advanced Light Source, which is a DOE Office of Science User Facility under Contract No. DE-AC02-05CH11231. We gratefully acknowledge the help of Oleg Kostko in setting up the VMI-XPS experiments at the Advanced Light Source, Emily Zhang for contributing towards setup of the THZ-TDS spectrometer, and Ishan Gupta for initial setup of the Irubis ATR device.

**References -**


1. Weng, L.; Stott, S. L.; Toner, M. Exploring Dynamics and Structure of Biomolecules, Cryoprotectants, and Water Using Molecular Dynamics Simulations: Implications for Biostabilization and Biopreservation. *Annu. Rev. Biomed. Eng.* **2019,** *21*, 1-31.
2. Meaney, P. M.; Fox, C. J.; Geimer, S. D.; Paulsen, K. D. Electrical Characterization of Glycerin: Water Mixtures: Implications for Use as a Coupling Medium in Microwave Tomography. *IEEE Trans. Microw. Theory Tech.* **2017,** *65* (5), 1471-1478.
3. Tellier, R. Review of aerosol transmission of influenza A virus. *Emerg Infect. Dis.* **2006,** *12* (11), 1657-62.
4. Anderson, E. L.; Turnham, P.; Griffin, J. R.; Clarke, C. C. Consideration of the Aerosol Transmission for COVID-19 and Public Health. *Risk. Anal.* **2020,** *40* (5), 902-907.
5. Zuo, Y. Y.; Uspal, W. E.; Wei, T. Airborne Transmission of COVID-19: Aerosol Dispersion, Lung Deposition, and Virus-Receptor Interactions. *ACS Nano.* **2020,** *14* (12), 16502-16524.
6. Ingebrethsen, B. J.; Cole, S. K.; Alderman, S. L. Electronic cigarette aerosol particle size distribution measurements. *Inhal. Toxicol.* **2012,** *24* (14), 976-84.
7. Nordlund, M.; Kuczaj, A. K. Modeling aerosol formation in an electrically heated tobacco product. *International Journal of Chemical, Molecular, Nuclear, Materials and Metallurgical Engineering* **2016,** *10* (4), 358-370.
8. Wright, T. P.; Song, C.; Sears, S.; Petters, M. D. Thermodynamic and kinetic behavior of glycerol aerosol. *Aerosol Sci. Technol.* **2016,** *50* (12), 1385-1396.
9. Murata, K.; Tanaka, H. Liquid-liquid transition without macroscopic phase separation in a water-glycerol mixture. *Nat. Mater* **2012,** *11* (5), 436-43.
10. Shin, S.; Jacobi, I.; Stone, H. A. Bénard-Marangoni instability driven by moisture absorption. *EPL (Europhysics Letters)* **2016,** *113* (2), 24002.
11. Jensen, M. H.; Gainaru, C.; Alba-Simionesco, C.; Hecksher, T.; Niss, K. Slow rheological mode in glycerol and glycerol-water mixtures. *Phys. Chem. Chem. Phys.* **2018,** *20* (3), 1716-1723.
12. Abou-Saleh, R. H.; McLaughlan, J. R.; Bushby, R. J.; Johnson, B. R.; Freear, S.; Evans, S. D.; Thomson, N. H. Molecular Effects of Glycerol on Lipid Monolayers at the Gas-Liquid Interface: Impact on Microbubble Physical and Mechanical Properties. *Langmuir* **2019,** *35* (31), 10097-10105.
13. Towey, J. J.; Soper, A. K.; Dougan, L. Molecular insight into the hydrogen bonding and micro-segregation of a cryoprotectant molecule. *J. Phys. Chem. B* **2012,** *116* (47), 13898-904.
14. Towey, J. J.; Soper, A. K.; Dougan, L. Low-Density Water Structure Observed in a Nanosegregated Cryoprotectant Solution at Low Temperatures from 285 to 238 K. *J. Phys. Chem. B* **2016,** *120* (19), 4439-48.
15. Zelent, B.; Nucci, N. V.; Vanderkooi, J. M. Liquid and Ice Water and Glycerol/Water Glasses Compared by Infrared Spectroscopy from 295 to 12 K. *J. Phys. Chem. A* **2004,** *108* (50), 11141-11150.
16. Dashnau, J. L.; Nucci, N. V.; Sharp, K. A.; Vanderkooi, J. M. Hydrogen bonding and the cryoprotective properties of glycerol/water mixtures. *J. Phys. Chem. B* **2006,** *110* (27), 13670-7.
17. Kataoka, Y.; Kitadai, N.; Hisatomi, O.; Nakashima, S. Nature of hydrogen bonding of water molecules in aqueous solutions of glycerol by attenuated total reflection (ATR) infrared spectroscopy. *Appl. Spectrosc.* **2011,** *65* (4), 436-41.
18. Behrends, R.; Fuchs, K.; Kaatze, U.; Hayashi, Y.; Feldman, Y. Dielectric properties of glycerol/water mixtures at temperatures between 10 and 50 degrees C. *J. Chem. Phys.* **2006,** *124* (14), 144512.
19. Hayashi, Y.; Puzenko, A.; Feldman, Y. Slow and fast dynamics in glycerol–water mixtures. *J. Non-Cryst. Solids* **2006,** *352* (42-49), 4696-4703.

20. Mallamace, F.; Corsaro, C.; Mallamace, D.; Vasi, C.; Vasi, S.; Stanley, H. E. Some Considerations on Confined Water: The Thermal Behavior of Transport Properties in Water-Glycerol and Water-Methanol Mixtures. *MRS Advances* **2016,** *1* (26), 1891-1902.
21. Charkhesht, A.; Lou, D.; Sindle, B.; Wen, C.; Cheng, S.; Vinh, N. Q. Insights into Hydration Dynamics and Cooperative Interactions in Glycerol-Water Mixtures by Terahertz Dielectric Spectroscopy. *J. Phys. Chem. B* **2019,** *123* (41), 8791-8799.
22. Kuhnhold, A.; Meyer, H.; Amati, G.; Pelagejcev, P.; Schilling, T. Derivation of an exact, nonequilibrium framework for nucleation: Nucleation is a priori neither diffusive nor Markovian. *Phys. Rev. E* **2019,** *100* (5-1), 052140.
23. Davies, J. F.; Haddrell, A. E.; Reid, J. P. Time-Resolved Measurements of the Evaporation of Volatile Components from Single Aerosol Droplets. *Aerosol Sci. Tech.* **2012,** *46* (6), 666-677.
24. Gao, X.; Cai, C.; Ma, J.; Zhang, Y. Repartitioning of glycerol between levitated and surrounding deposited glycerol/NaNO3/H2O droplets. *R. Soc. Open Sci.* **2018,** *5* (1), 170819.
25. Frege, C.; Asgari, M.; Steiner, S.; Ferreira, S.; Majeed, S.; Lucci, F.; Frentzel, S.; Hoeng, J.; Kuczaj, A. K. Assessment of Single-Photon Ionization Mass Spectrometry for Online Monitoring of in Vitro Aerosol Exposure Experiments. *Chem. Res. Toxicol.* **2020,** *33* (2), 505-514.
26. David, G.; Parmentier, E. A.; Taurino, I.; Signorell, R. Tracing the composition of single e-cigarette aerosol droplets in situ by laser-trapping and Raman scattering. *Sci. Rep.* **2020,** *10* (1), 7929.
27. Signorell, R.; Goldmann, M.; Yoder, B. L.; Bodi, A.; Chasovskikh, E.; Lang, L.; Luckhaus, D. Nanofocusing, shadowing, and electron mean free path in the photoemission from aerosol droplets. *Chem. Phys. Lett.* **2016,** *658*, 1-6.
28. Xu, B.; Jacobs, M. I.; Kostko, O.; Ahmed, M. Guanidinium Group Remains Protonated in a Strongly Basic Arginine Solution. *Chem. Phys. Chem.* **2017,** *18* (12), 1503-1506.
29. Kostko, O.; Xu, B.; Ahmed, M. Local electronic structure of histidine in aqueous solution. *Phys. Chem. Chem. Phys.* **2021,** *23* (14), 8847-8853.
30. Kostko, O.; Jacobs, M. I.; Xu, B.; Wilson, K. R.; Ahmed, M. Velocity map imaging of inelastic and elastic low energy electron scattering in organic nanoparticles. *J. Chem. Phys.* **2019,** *151* (18), 184702.
31. Kostko, O.; Xu, B.; Jacobs, M. I.; Ahmed, M. Soft X-ray spectroscopy of nanoparticles by velocity map imaging. *J. Chem. Phys.* **2017,** *147* (1), 013931.
32. Lee, M. T.; Orlando, F.; Artiglia, L.; Chen, S.; Ammann, M. Chemical Composition and Properties of the Liquid-Vapor Interface of Aqueous C1 to C4 Monofunctional Acid and Alcohol Solutions. *J. Phys. Chem. A* **2016,** *120* (49), 9749-9758.
33. Walz, M. M.; Werner, J.; Ekholm, V.; Prisle, N. L.; Ohrwall, G.; Bjorneholm, O. Alcohols at the aqueous surface: chain length and isomer effects. *Phys. Chem. Chem. Phys.* **2016,** *18* (9), 6648-56.
34. Marinho, R. R. T.; Walz, M. M.; Ekholm, V.; Ohrwall, G.; Bjorneholm, O.; de Brito, A. N. Ethanol Solvation in Water Studied on a Molecular Scale by Photoelectron Spectroscopy. *J. Phys. Chem. B* **2017,** *121* (33), 7916-7923.
35. Newberg, J. T.; Bluhm, H. Adsorption of 2-propanol on ice probed by ambient pressure X-ray photoelectron spectroscopy. *Phys. Chem. Chem. Phys.* **2015,** *17* (36), 23554-8.
36. Nagasaka, M.; Mochizuki, K.; Leloup, V.; Kosugi, N. Local structures of methanol-water binary solutions studied by soft X-ray absorption spectroscopy. *J. Phys. Chem. B* **2014,** *118* (16), 4388-96.
37. Lam, R. K.; Smith, J. W.; Saykally, R. J. Communication: Hydrogen bonding interactions in water-alcohol mixtures from X-ray absorption spectroscopy. *J. Chem. Phys.* **2016,** *144* (19), 191103.
38. Juurinen, I.; Pylkkanen, T.; Sahle, C. J.; Simonelli, L.; Hamalainen, K.; Huotari, S.; Hakala, M. Effect of the hydrophobic alcohol chain length on the hydrogen-bond network of water. *J. Phys. Chem. B* **2014,** *118* (29), 8750-5.

39. Pellegrin, E.; Perez-Dieste, V.; Escudero, C.; Rejmak, P.; Gonzalez, N.; Fontsere, A.; Prat, J.; Fraxedas, J.; Ferrer, S. Water/methanol solutions characterized by liquid μ-jet XPS and DFT—The methanol hydration case. *J. Mol. Liq.* **2020,** *300*, 112258.
40. Stetina, T. F.; Clark, A. E.; Li, X. X-ray absorption signatures of hydrogen-bond structure in water-alcohol solutions. *Int. J. Quantum Chem.* **2019,** *119* (1), e25802.
41. Li, R.; D'Agostino, C.; McGregor, J.; Mantle, M. D.; Zeitler, J. A.; Gladden, L. F. Mesoscopic structuring and dynamics of alcohol/water solutions probed by terahertz time-domain spectroscopy and pulsed field gradient nuclear magnetic resonance. *J. Phys. Chem. B* **2014,** *118* (34), 10156-66.
42. Tan, N. Y.; Li, R.; Brauer, P.; D'Agostino, C.; Gladden, L. F.; Zeitler, J. A. Probing hydrogen-bonding in binary liquid mixtures with terahertz time-domain spectroscopy: a comparison of Debye and absorption analysis. *Phys. Chem. Chem. Phys.* **2015,** *17* (8), 5999-6008.
43. Habuka, A.; Yamada, T.; Nakashima, S. Interactions of Glycerol, Diglycerol, and Water Studied Using Attenuated Total Reflection Infrared Spectroscopy. *Appl. Spectrosc.* **2020,** *74* (7), 767-779.
44. Besley, N. A. Modeling of the spectroscopy of core electrons with density functional theory. **2021**, *WIREs Comput. Mol. Sci.e1527.*
45. Gozem, S.; Seidel, R.; Hergenhahn, U.; Lugovoy, E.; Abel, B.; Winter, B.; Krylov, A. I.; Bradforth, S. E. Probing the Electronic Structure of Bulk Water at the Molecular Length Scale with Angle-Resolved Photoelectron Spectroscopy. *J. Phys. Chem. Lett.* **2020,** *11* (13), 5162-5170.
46. Sadybekov, A.; Krylov, A. I. Coupled-cluster based approach for core-level states in condensed phase: Theory and application to different protonated forms of aqueous glycine. *J. Chem. Phys.* **2017,** *147* (1), 014107.
47. Hartweg, S.; Garcia, G. A.; Bozanic, D. K.; Nahon, L. Condensation Effects on Electron Chiral Asymmetries in the Photoionization of Serine: From Free Molecules to Nanoparticles. *J. Phys. Chem. Lett.* **2021,** *12* (9), 2385-2393.
48. Silva, J. L.; Unger, I.; Matias, T. A.; Franco, L. R.; Damas, G.; Costa, L. T.; Toledo, K. C. F.; Rocha, T. C. R.; de Brito, A. N.; Saak, C. M.; Coutinho, K.; Araki, K.; Bjorneholm, O.; Brena, B.; Araujo, C. M. X-ray Photoelectron Fingerprints of High-Valence Ruthenium-Oxo Complexes along the Oxidation Reaction Pathway in an Aqueous Environment. *J. Phys. Chem. Lett.* **2019,** *10* (24), 7636-7643.
49. Oh, K. I.; Baiz, C. R. Molecular heterogeneity in aqueous cosolvent systems. *J. Chem. Phys.* **2020,** *152* (19), 190901.
50. Li, B.; Kawakita, Y.; Ohira-Kawamura, S.; Sugahara, T.; Wang, H.; Wang, J.; Chen, Y.; Kawaguchi, S. I.; Kawaguchi, S.; Ohara, K.; Li, K.; Yu, D.; Mole, R.; Hattori, T.; Kikuchi, T.; Yano, S. I.; Zhang, Z.; Zhang, Z.; Ren, W.; Lin, S.; Sakata, O.; Nakajima, K.; Zhang, Z. Colossal barocaloric effects in plastic crystals. *Nature* **2019,** *567* (7749), 506-510.
51. Jacobs, M. I.; Xu, B.; Kostko, O.; Wiegel, A. A.; Houle, F. A.; Ahmed, M.; Wilson, K. R. Using Nanoparticle X-ray Spectroscopy to Probe the Formation of Reactive Chemical Gradients in Diffusion-Limited Aerosols. *J. Phys. Chem. A* **2019,** *123* (28), 6034-6044.
52. Wei, Z.; Li, Y.; Cooks, R. G.; Yan, X. Accelerated Reaction Kinetics in Microdroplets: Overview and Recent Developments. *Annu. Rev. Phys. Chem.* **2020,** *71*, 31-51.
53. Rovelli, G.; Jacobs, M. I.; Willis, M. D.; Rapf, R. J.; Prophet, A. M.; Wilson, K. R. A critical analysis of electrospray techniques for the determination of accelerated rates and mechanisms of chemical reactions in droplets. *Chem. Sci.* **2020,** *11* (48), 13026-13043.
54. Wilson, K. R.; Prophet, A. M.; Rovelli, G.; Willis, M. D.; Rapf, R. J.; Jacobs, M. I. A kinetic description of how interfaces accelerate reactions in micro-compartments. *Chem. Sci.* **2020,** *11* (32), 8533-8545.
55. Dribinski, V.; Ossadtchi, A.; Mandelshtam, V. A.; Reisler, H. Reconstruction of Abel-transformable images: The Gaussian basis-set expansion Abel transform method. *Rev. Sci. Instrum.* **2002,** *73* (7), 2634-2642.